Computational Geosciences manuscript No.
(will be inserted by the editor)

Field-scale modeling of microbially induced calcite precipitation

A.B. Cunningham · H. Class · A. Ebigbo · R. Gerlach · A.J. Phillips · J. Hommel

Received: date / Accepted: date

Abstract The biogeochemical process known as microbially induced calcite precipitation (MICP) is being investigated for engineering and material science applications. To model MICP process behavior in porous media, computational simulators must couple flow, transport, and relevant biogeochemical reactions. Changes in media porosity and permeability due to biomass growth and calcite precipitation, as well as their effects on one another must be considered. A comprehensive Darcy-scale model has been developed by Ebigbo et al (2012) and Hommel et al (2015) and validated at different scales of observation using laboratory experimental systems at the Center for Biofilm Engineering (CBE), Montana State University (MSU). This investigation clearly demonstrates that a close synergy between laboratory experimentation at different scales and corresponding simulation model development is necessary to advance MICP application to the field scale. Ultimately, model predictions of MICP sealing of a fractured sandstone formation, located 340.8 m below ground surface, were made and compared with corresponding field observations. Modeling MICP at the field scale poses special challenges, including choosing a reasonable model-domain size, initial and boundary conditions, and determining the initial distribution of porosity and permeability. In the presented study, model predictions of deposited calcite volume agree favorably with corresponding field observations of increased injection pressure during the MICP fracture sealing test in the field. Results indicate that the current status of our MICP model now allows its use for further subsurface engineering applications, including well-bore-cement sealing and certain fracture-related applications in unconventional oil and gas production.

A.B. Cunningham
Center for Biofilm Engineering, Montana State University, 366 Barnard Hall, Bozeman, MT 59717, USA

H. Class
Department of Hydromechanics and Modelling of Hydrosystems, University of Stuttgart, Pfaffenwaldring 61, 70569 Stuttgart, Germany

A. Ebigbo
Institute of Geophysics, Swiss Federal Institute of Technology Zurich, Sonneggstrasse 5, 8092 Zurich, Switzerland

R. Gerlach
Center for Biofilm Engineering, Montana State University, 366 Barnard Hall, Bozeman, MT 59717, USA

A.J. Phillips
Center for Biofilm Engineering, Montana State University, 366 Barnard Hall, Bozeman, MT 59717, USA

J. Hommel
Department of Hydromechanics and Modelling of Hydrosystems, University of Stuttgart, Pfaffenwaldring 61, 70569 Stuttgart, Germany
Tel.: +49-711-68564600
Fax: +49-711-68560430
E-mail: johannes.hommel@iws.uni-stuttgart.de

Keywords microbially induced calcite precipitation (MICP) · permeability modification · field-scale modeling · reactive transport

1 Introduction

Microbially induced calcite precipitation (MICP) is becoming established as a useful technology for a range of geoscience and engineering applications, as summarized by Phillips et al (2013a), including amending or improving construction materials, cementing porous media, environmental remediation, and containment of nuclear waste. In the subsurface environment, MICP causes deposition of calcium carbonate, resulting in a reduction of porosity and permeability. For example, MICP minerals deposited in preferential flow paths in fractured porous media, and in the near-well-bore environment can mitigate leakage potential of sequestered carbon dioxide, methane, and well-bore fluids (Phillips et al, 2013b; Mitchell et al, 2013). MICP technology is based on the injection of relatively low-viscosity aqueous solutions which promote calcite precipitation to seal unwanted flow paths, especially in small aperture fractures. MICP therefore compliments traditional high-viscosity sealants (e.g. cement) used to seal unwanted flow paths in the near-well-bore environment.

To better understand and predict MICP process behavior in porous media systems, computational simulators must be developed which couple flow, transport, and biogeochemical reactions. Changes in media porosity and permeability need to be considered and coupled to biomass growth and calcite precipitation. A comprehensive model has been developed by the University of Stuttgart and partners and validated at different scales of observation using laboratory experimental systems at the Center for Biofilm Engineering (CBE), Montana State University (MSU) (Ebigbo et al, 2010, 2012; Hommel et al, 2015, 2016). Ultimately, model predictions of MICP sealing of a fractured sandstone formation, located 340.8 m below ground surface, were made and compared with actual field experiments which resulted in virtually complete fracture sealing. Results indicate that, even though parts of the current MICP model are still considered as work in progress, it might now be suitable for other types of important subsurface field-scale applications, including well-bore-cement sealing and certain unconventional oil- and gas-related applications. Field experiments in both of these areas are now beginning.

Below, we review briefly the major fundamentals of microbially induced calcite precipitation, while referring, for details, to our previous publications in this field. Subsequently, we summarize the history of the development of our mathematical and numerical model, thereby discussing the different scales and the importance of experimental results for step wise validation of the model. The core part of this paper is then the presentation of the field demonstration, its modeling, and the discussion of the results of this study. This allows us to draw conclusions on the current state of the model and on perspectives on its application in future work.

2 MICP Fundamentals

Microbially induced calcite precipitation (MICP) occurs when microbial metabolism alters the surrounding aqueous phase in a way that leads to precipitation of calcite. In this study, we focus on biofilm-based MICP via ureolysis by the bacterium *Sporosarcina pasteurii*. MICP offers an engineering option that uses controlled biofilm growth to achieve targeted calcite precipitation, which can be employed in various applications (e.g. Krajewska, 2017; Umar et al, 2016; Phillips et al, 2013a). In subsurface applications, this process is typically associated with a reduction of porosity and, even more importantly, of permeability (e.g. Cuthbert et al, 2013; Whiffin et al, 2007; Nemati and Voordouw, 2003; Ferris et al, 1996). For example Minto et al (2018) show the reduction in permeability also by solving the Navier-Stokes equation on the geometry extracted from X-ray computed tomography of samples before and after MICP treatment. *S. pasteurii* expresses the enzyme urease that catalyzes the hydrolysis reaction of urea ($CO(NH_2)_2$) into ammonia (NH_3) and carbon dioxide (CO_2) (e.g. Bachmeier et al, 2002). Aqueous solutions of ammonia become alkaline. Thus, the ureolysis reaction leads to an increase in alkalinity. This shifts the carbonate balance in an aqueous solution toward higher concentrations of dissolved carbonate (${CO_3}^{2-}$). Adding calcium (Ca^{2+}) to the system then results in the precipitation of calcium carbonate ($CaCO_3$).

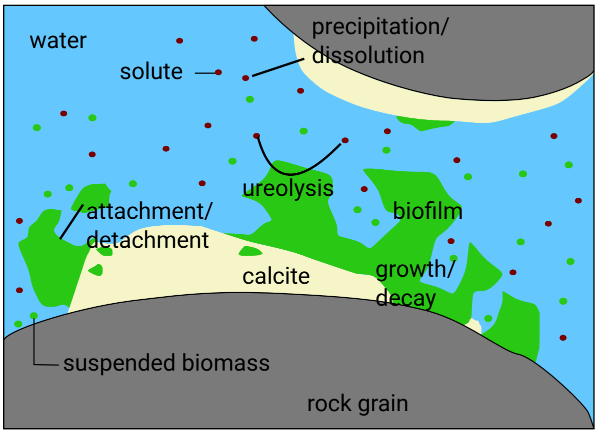

Fig. 1 Schematic view of relevant processes and phases considered in the conceptual MICP model for the field application scenario, modified from Hommel et al (2015).

$$CO(NH_2)_2 + 2\,H_2O + Ca^{2+} \longrightarrow 2\,{NH_4}^{+} + CaCO_3\downarrow . \quad (1)$$

Figure 1 illustrates the main processes governing MICP at the pore scale. Ureolytically active *S. pasteurii* cells are introduced in aqueous suspension. These cells attach to surfaces, take up nutrients, and form a biofilm. As biofilm growth continues, some cells detach and are transported down gradient. A detailed discussion of biofilm processes in porous media appears in Ebigbo et al (2010). The MICP process continues with the addition of urea which is hydrolyzed, resulting in a pH increase. Subsequent addition of Ca^{2+} results in calcium carbonate (calcite) deposition, which, together with the accumulated biofilm, causes a reduction in porosity and permeability of the porous medium.

Figure 2 shows a visual example of calcite deposition resulting from the MICP process. In this example, MICP was applied to seal a horizontal fracture in a 76.2 cm-diameter sandstone core as reported by Phillips et al (2015). These meso-scale laboratory experiments provided valuable insights into the formulation of a protocol for the injection of media for MICP, including microbial inoculum, urea, and calcium in order to achieve virtually complete sealing of the fracture under radial flow conditions. Modeling of these experiments as an intermediate step before modeling the field-scale application is discussed below in Section 3.3.

3 Model Development

The major challenge in constructing a predictive model for permeability reduction in the underground with MICP is quantifying the complex interactions between flow, transport, biofilm growth, and reaction kinetics. Any model for MICP, or, more generally, reactive transport, is necessarily a simplification of these processes and their interactions and any new experimental insight into the processes has the potential to improve such models. Thus, there exists a variety of numerical models for reactive transport in porous media which involve microbial activity. Applications found in the literature include the interaction of microbes with the subsurface transport of contaminants, (e.g. Jacques et al, 2008; Prommer et al, 2007; Watson et al, 2003; Tebes-Stevens et al, 1998), microbially enhanced oil recovery (e.g. Landa-Marbán et al, 2017; Nielsen et al, 2016, 2014; Vilcáez et al, 2013) or biomineralization, of which especially the engineered application of microbially induced calcite precipitation (MICP) has received considerable attention. Most numerical models for MICP are, similarly to the model used in this study, formulated at the REV scale (or: Darcy scale) (e.g. Barkouki et al, 2011; Cuthbert et al, 2013; Martinez et al, 2014; Nassar et al, 2018; van Wijngaarden et al, 2011, 2013, 2016), while Qin et al (2016) and Zhang and Klapper (2010, 2011, 2014) use pore-network and pore-scale models, respectively.

Many models are designed to match some experiments, focusing on the processes of relevance in the particular experiments while neglecting other processes that might be relevant at the field scale. The models presented by Martinez et al (2014) and Barkouki et al (2011) use a complex ureolysis rate equation (Fidaleo and Lavecchia, 2003), the same as our initial model (Ebigbo et al, 2012), and a saturation-state dependent precipitation rate, while neglecting changes in permeability and assuming a constant biomass distribution. This results in a constant ureolytic activity over time for each point. Cuthbert et al (2013) use a first-order kinetic model for ureolysis and model bacterial transport and attachment. However, they simplified the geochemistry by setting the precipitation rate equal to the ureolysis rate. On the other hand, they account for the impact of the calcite precipitated during MICP on hydrodynamics. Michaelis-Menten kinetics are used to model the ureolysis rate in van Wijngaarden et al (2011, 2013, 2016) and, like Cuthbert et al (2013), they assume that the precipitation rate is proportional to the ureolysis rate. The permeability change is accounted for by a Kozeny-Carman relationship, but only calcite is assumed to have an effect. Bacteria are assumed to be homogeneously distributed in van Wijngaarden et al (2011), while van Wijngaarden et al (2013) account for attachment, detachment, and bacterial transport and van Wijngaarden et al (2016) investigate the effect of various decay and biomass removal rates. For special cases, van Wijngaarden et al (2011, 2013) propose analytical solutions. The kinetic rate equations, in Qin et al (2016) are identical to those used in our modified model (Hommel et al, 2015).

3.1 Brief Presentation of MICP Model Equations

The initial model for MICP published by Ebigbo et al (2012) was developed based on the final calcite distribution from four quasi-1D column experiments. It, and its improvement by Hommel et al (2015), is to our knowledge the most complex numerical model for MICP that has been published, including a fairly complex solution chemistry, growth, decay, attachment, detachment, transport of biomass, detailed kinetic rate equations for the biomass processes, ureolysis, precipitation and dissolution of calcite, effects of both biofilm and calcite on porosity and permeability, and the possibility to account for two-phase flow. The model is based on standard mass balance equations for each dissolved component (water (w), inorganic carbon (ic), sodium (Na), chloride (Cl), calcium (Ca), urea (u), ammonium/ammonia (a), substrate (s), oxygen (O_2), and suspended biomass(sb)) and solid phase (biofilm (b) and calcite (c)), using Darcy's law for the phase velocities. Primary variables are the phase pressure, the mole

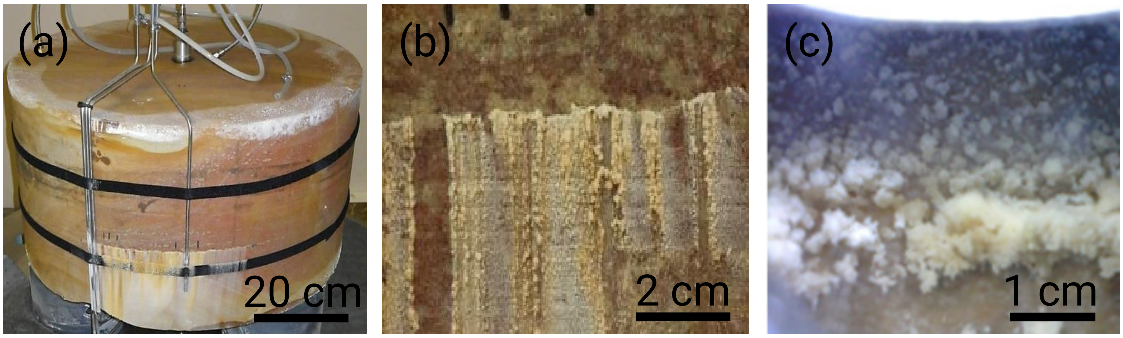

Fig. 2 Precipitates observed from MICP sealing of a 1 mm fracture (33 cm in length) in a 76.2 cm diameter sandstone core. (a, b) Precipitates formed in the region of the fracture; (c) Precipitates were observed inside the 5.4 cm diameter stainless steel injection tube. These photographs help visualize the nature of the mineral deposits resulting from the application of MICP to seal fractured porous media.

fractions of the components, and the volume fractions of the solid phases.

$$\sum_\alpha \frac{\partial}{\partial t}\left(\phi \rho_\alpha x_\alpha^\kappa S_\alpha\right) + \nabla\cdot\left(\rho_\alpha x_\alpha^\kappa \mathbf{v}_\alpha\right) \\ -\nabla\cdot\left(\rho_\alpha \mathbf{D}_{\mathrm{pm},\alpha} \nabla x_\alpha^\kappa\right) = q^\kappa, \tag{2}$$

here, t is time, ϕ porosity, ρ_α, S_α, and $\mathbf{v}_\alpha$ the density, saturation and the velocity of phase α respectively, x_α^κ the mole fraction of component κ in phase α. $\mathbf{D}_{\mathrm{pm},\alpha}$ is the dispersion tensor of phase α in the porous medium, and q^κ is the source term of component κ due to biogeochemical reactions. The mass balances for the solid phases calcite (c) and biofilm (b) contain only a storage and source term since they are immobile:

$$\frac{\partial}{\partial t}\left(\phi_\lambda \rho_\lambda\right) = q^\lambda, \tag{3}$$

here, ϕ_λ and ρ_λ are volume fraction and density of the solid phase λ, and q^λ is the source term of phase λ due to biochemical reactions. The mass balance equations for the transported components (Eq. (2)) and the solid phases (Eq. (3)) are coupled by the component-specific reactive source and sink terms q^κ and q^λ, which are discussed in detail in Ebigbo et al (2012) and Hommel et al (2015). The porosity is updated by subtracting the solid-phase volume fractions ϕ_λ from the initial porosity ϕ_0:

$$\phi = \phi_0 - \sum_i \phi_i = \phi_0 - \phi_\mathrm{b} - \phi_\mathrm{c}. \tag{4}$$

As both the volume fraction of biofilm ϕ_b and calcite ϕ_c are assumed to be impermeable, the permeability K can be calculated using the porosity from Equation (4), without distinguishing between the contribution of each solid. To relate the changes in porosity to the change in permeability, a Verma–Pruess type relation (Verma and Pruess, 1988) with an exponent of 3 is chosen, reducing the effective porosity by the parameter of the critical porosity ϕ_crit, at and below which the permeability becomes zero even though a residual porosity persists:

$$\frac{K}{K_0} = \left[\frac{(\phi - \phi_\mathrm{crit})}{(\phi_0 - \phi_\mathrm{crit})}\right]^3. \tag{5}$$

The model is implemented in the open-source simulator DuMu$^\mathrm{X}$ (DUNE for Multi-Phase, Component, Scale, Physics, . . .) (Flemisch et al, 2011), which is based on DUNE (Distributed and Unified Numerics Environment) which, itself, is an open-source framework for solving partial differential equations (Bastian et al, 2008b,a). This study uses as discretization methods implicit Euler for time and a fully coupled, vertex-centered finite volume (box) scheme (Helmig, 1997) for space. The resulting system of equations is solved using the BiCGStab solver (van der Vorst, 1992) after being linearized using the Newton-Raphson method. The time stepping is adaptive and the size for each time step is determined by the number of Newton iterations until convergence of the previous time step and its size. In case the Newton-Raphson method does not converge within a maximum number of iterations, the time step is restarted with half the initial time-step size.

A comprehensive discussion of the MICP model, especially the individual reactive source and sink terms, the capability for including a potential second fluid phase, and the treatment of equilibrium dissociation reactions, is given in Ebigbo et al (2012) and Hommel et al (2015). For convenience, we summarize the reactive source and sink terms, the reaction rate equations, the model parameters used, and the initial and boundary conditions in the Appendix.

3.2 How the Model was Improved by Experiments

In Hommel et al (2015), the MICP model was improved based on new insights regarding the main driving force of the MICP reactions, urea hydrolysis. Experiments with *S. pasteurii*, the organism mostly used for engineered MICP research and development, allowed us the determination of whole-cell ureolysis kinetics parameters (Lauchnor et al, 2015). This in turn allowed for the implementation of more appropriate ureolysis rate kinetics in the reactive source and sink terms associated with ureolysis.

Simultaneous to the investigation of the ureolysis kinetics, new column experiments were conducted monitoring Ca^{2+} and $NH_4{}^+$ concentrations at 10 cm intervals along the column over time to provide improved experimental data for recalibration of the model by inverse modeling (Hommel et al, 2015). This significantly increased the experimental data available for calibration compared to the previous experiments, were only the final amount of calcite along the column was available (Ebigbo et al, 2012). The updated and recalibrated model was validated using data of the replicate of the new column experiment, again with Ca^{2+} and $NH_4{}^+$ concentration and final calcite measurements, as well as a previous experiment described in Ebigbo et al (2012) (Hommel et al, 2015). The improved model proved to be more robust with respect to the medium chemistry, which changed between the experiments reported in Ebigbo et al (2012) and Hommel et al (2015), increasing its predictive capabilities. However, the model was, up to that point, almost exclusively validated with data from quasi-1D column experiments with plug-flow conditions. Thus, a comparison between model predictions and experimental data in a full 3D setup with radial flow conditions was conducted before the model was applied to investigate a field-scale scenario. Figure 3 provides a summary of the interaction between laboratory experimentation and model development.

3.3 Transition from Laboratory to Field-relevant Applications

The model published by Ebigbo et al (2012) and Hommel et al (2015) was essentially validated using quasi-1D column experimental data and one 2D radial flow data set. Additionally, in all of the previous experiments, the porous medium had been homogeneous sand. Therefore, as the next step toward field application, we investigated the model's capability to predict radial flow in a 3D domain in a field-relevant porous medium (sandstone). To this end, we simulated MICP sealing in the medium-scale sandstone through the experiments by Phillips et al (2015) (summarized in Figure 2), which featured a horizontal fracture and horizontal flow conditions. The model and parameters used were those published in Ebigbo et al (2012), as the simulation was carried out in 2013, before the model was improved and recalibrated by Hommel et al (2015) (see Section 3.2). This horizontal sandstone fracture experiment was very similar to the conditions encountered in the MICP field demonstration described in Section 4. The setup, initial and boundary conditions for the simulation were taken from Phillips et al (2015). The boundary conditions are chosen as no-flow conditions except for Dirichlet conditions at the outer radius and the top and the injection at the inner radius according to Phillips et al (2015). The simulation showed that the model was able to simulate 3D domains, although the computational costs are high. The model results (Figure 4) show preferential biomass accumulation in the high-permeable layer at the bottom of the simulation domain representing the fracture in the sandstone core. This leads to preferential precipitation within this layer, eventually sealing the fracture as also observed in the experiments by Phillips et al (2015) summarized in Figure 2. A detailed discussion of the results for this modeling effort is beyond the scope of this article. However, there was good qualitative agreement between simulation results and experimental observations, which increased our confidence that the model could be applied to similar conditions at the field site without significant further modification.

4 Modeling MICP at the Field Scale

A subsurface sandstone fracture-sealing field demonstration was conducted in April 2014. Collaborators on this field-scale demonstration include the Center for Biofilm Engineering at Montana State University (CBE/MSU), Southern Company (SC), the University of Alabama at Birmingham (UAB), Schlumberger Carbon Services (SLB), Shell International Exploration and Production B.V. (Shell), and the University of Stuttgart (Stuttgart). CBE/MSU designed the field demonstration protocol, oversaw testing and analyzed results. Stuttgart supervised numerical modeling in collaboration with CBE researchers. Southern Company conducted geologic site characterization and obtained rock core samples from the field for laboratory analysis. SC also helped coordinate field operations with Schlumberger. UAB conducted multiple core tests on field and laboratory sandstone rock core samples. Shell assisted in designing the field demonstration and analyzing results. All collaborators actively participated in decision-making and evaluation for each stage of the project. This project integrated expertise from practitioners (SC, SLB, and

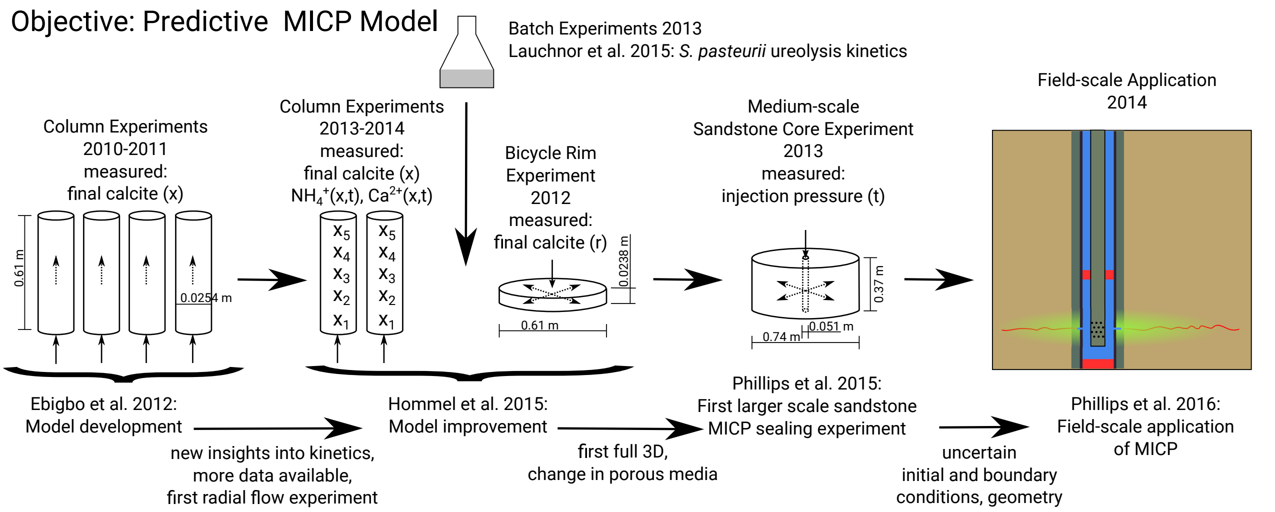

Fig. 3 Model and experiment development involved in preparation for the field-scale application.

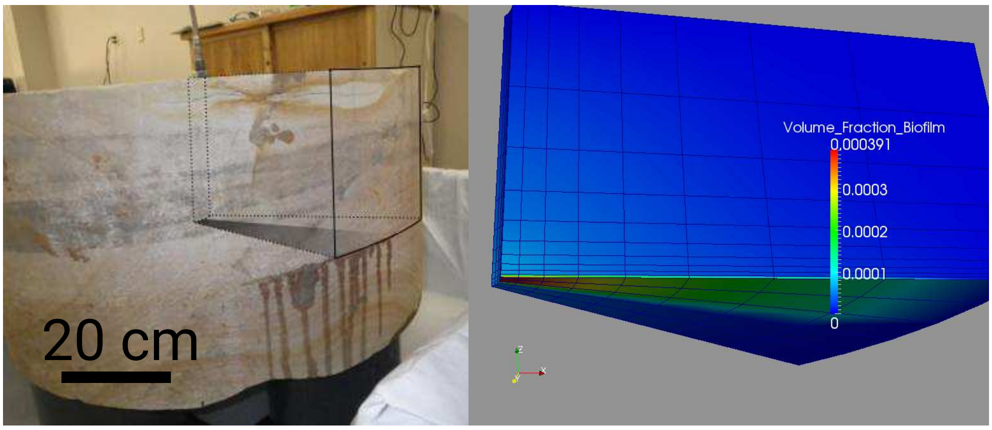

Fig. 4 MICP modeling of the sandstone-core experiment from Figure 2: (Left) picture of the fractured meso-scale core and a sketch of the simulation domain with the shaded area as the highly permeable layer representing the fracture; the darker areas are indicative of fluids exiting the horizontal fracture. (Right) model prediction of biofilm distribution after 1.16 d of injection. Most of the biofilm is concentrated in the fracture at the front and bottom of the domain.

Shell) with experimental research (MSU/CBE, UAB) and numerical modeling (Stuttgart) to successfully complete the field demonstration thoroughly evaluating the field injection protocol, field delivery system, and effectiveness of the biomineralization sealing process. Herein we highlight the role of numerical modeling at Stuttgart.

4.1 Description of the MICP Sealing Field Demonstration

Previously reported MICP-related field studies include stimulation of microbial urea hydrolysis in groundwater to enhance calcite precipitation, Fujita et al (2008), using MICP to reduce permeability of fractured volcanic rock at a 25 m depth, Cuthbert et al (2013), and precipitation of calcite by indigenous microorganisms to strengthen liquefiable soils, Burbank et al (2011). Another noteworthy large-scale MICP experiment which quantified biomediated ground improvement by ureolysis is reported by van Paassen et al (2010). The MICP sealing field study discussed herein builds on these previous field-scale studies by demonstrating the use of MICP in fractured sandstone 340.8 m below ground surface (bgs) using conventional oil-field delivery techniques.

The MICP sealing field demonstration was performed inside a 24.4 cm-diameter well located on the Gorgas Steam Generation facility near Jasper, Alabama, USA (hereafter referred to as the Gorgas site). The target zone for the sealing experiment was a horizontal sandstone fracture, located 340.8 m bgs.

The field demonstration involved the following sequence: (1) field-site characterization; (2) fracturing the sandstone formation to develop injectivity; (3) design of a protocol for field injection strategy; (4) injection of microbes, urea, and calcium in the field using conventional oil-field delivery technologies; and (5) assessment of the fracture plugging after treatment. This sequence was described in detail in Phillips et al (2016).

Site Description: Based on a review of the petrophysical well logs for the site prepared by Schlumberger, the Fayette sandstone group at a depth of 338.3 to 341.4 m bgs was determined to be the best candidate for performing the field demonstration. The Fayette is a sandstone with, at this location, a porosity of approximately 12% and a permeability of $\sim 1.0856 \times 10^{-14}\mathrm{m}^2$ (11 mD), according to the pre-application petrophysical analysis by Schlumberger. The cement bond log (not shown) indicated good cement across the zone, so good hydraulic isolation was expected. Prior to the actual biomineralization sealing test, a bridge plug was installed in the well at an elevation of 343.5 m bgs. This plug established the lower boundary of the injection zone for injection of test fluids. The completely cased well was perforated in the target region, 340.7 to 341.1 m bgs, and a packer was set to isolate the Fayette formation (Phillips et al, 2016).

Preliminary well testing established that the $1.0856 \times 10^{-14}\mathrm{m}^2$ permeability of the Fayette sandstone was too low to conduct a meaningful MICP test on the formation itself and, therefore, it was decided to hydraulically fracture the formation in order to increase injectivity. Hydraulic fracturing was carried out by Schlumberger and resulted in the establishment of a single horizontal fracture plane extending radially into the Fayette sandstone located 340.8 m bgs. This fracture plane was established as the target zone for subsequent MICP sealing activities.

MICP Field Test: The MICP field demonstration involved microbial inoculation of the formation with *S. pasteurii* combined with urea and calcium injections over the course of four days. Several months prior to the field demonstration, multiple scenarios were run with the MICP simulation model considering actual characteristics at the Gorgas site. These modeling results were used to plan the actual injection sequence of MICP components. We also considered well-bore mixing and transport into the formation in such a way as to encourage reaction and calcite precipitation in the formation as opposed to inside the well-bore. This involved determining the schedule and flow rates for injecting fluids both during and after bailer injection of MICP components. We also needed assurance that the time needed to develop the MICP seal of the fracture would be no longer than four days. The MICP modeling scenarios, together with pre-field-test laboratory experiments, provided an efficient process for screening alternatives which resulted in the "best predicted" field injection strategy. Based on these results, it was possible to estimate quantities of key components such as microbial inoculum, calcium, urea etc. needed for the field work. This a priori MICP modeling/experimentation effort proved extremely valuable in successfully completing this MICP based fracture sealing in the field.

During the actual field demonstration, a total of 24 calcium injections and six microbe injections were required over the four-day period to achieve complete sealing. Conventional oil-field methods were used to deliver the biomineralization components downhole by using an 11.4 l wireline dump bailer combined with periodic pumping of a brine solution into the fractured formation. The fractured region was considered completely sealed when it was no longer possible to inject fluids into the formation without exceeding the initial formation fracture pressure. On day 3, around 45 h after the first injections, a significant decrease in injectivity was observed and the flow rates had to be reduced during the fourth day to avoid exceeding the formation's fracture pressure. Sealing of the fracture with MICP was assessed through (i) the reduction of injectivity, (ii) decrease in pressure decay after well shut in, and (iii) detection of MICP byproducts including calcium carbonate ($CaCO_3$) in side-wall cores retrieved from 1.8 m above the fracture zone. Detailed results of this MICP field demonstration are presented in Phillips et al (2016).

4.2 Model Predictions and Evaluation

In this section, two categories of modeling scenarios are discussed. The first category, identified as the *2014 simulations*, refers to the modeling done prior to and immediately after the April 2014 field demonstration. The second category, identified as the *2018 simulations*, refers to recent modeling done after evaluating the results of the field demonstration. The main difference of the simulations are the sets of parameters used and that the *2018 simulations* consider infinite-acting pressure boundary conditions at the outer radius of the simulation domain.

As the model recalibration discussed in Hommel et al (2015) was not yet completed at the time of the first modeling study in 2014, the values for some model input parameters differed from those published there. Those parameter values are given in Table 1. All other parameter values are identical to those published in Hommel et al (2015). Thus, in addition to investigating the effect of an improved pressure boundary condition, the 2018 simulations were also aimed at highlighting the impact of the changed set of parameters

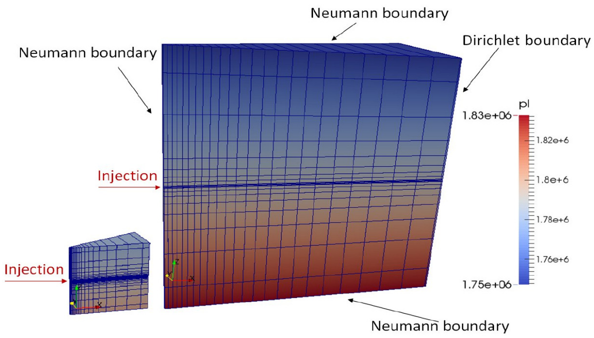

Fig. 5 Sketch of the grid for the 2.4 m×2.4 m and the 8 m×8 m and the initial pressure (in Pa) as well as the boundary conditions used for the 2014 simulations.

on the simulation results. No parameters were fitted for the field-scale simulations, as the *2014 simulations* were conducted prior to and immediately after the field application, when no data for calibration were available. Also for the *2018 simulations*, no parameters were fitted specifically for the field-application setup due to the scarcity of field-scale data.

Simulation Domains and Geometry: To address the uncertainty in the extent of the radial fracture, two scenarios were investigated prior to the 2014 field application: the "small" 2.4 m×2.4 m (height × radius) scenario with a radial fracture extent of 1.6 m and the "large" 8 m×8 m scenario with a radial fracture extent of 4 m. Both scenarios were simulated assuming various injection strategies (not shown or discussed here) and the best injection strategy was chosen to be used for the actual field test. For the recent simulations in 2018, the "large" scenario was extended to a radius of 50 m. As the vertical extent of the MICP sealing into the formation was part of the research question, it was necessary to use a 3D model and therefore not possible to reduce the domain to a 2D fracture plane. The simulation domains were constructed assuming radial symmetry with the domain height as well as the radial extent adjusted to the radial extent of the fracture, resulting in a height and radius of 2.4 m for the small and 8 m for the large scenario, see Figure 5. For each scenario, the fracture is approximated as a 5 cm thick highly permeable layer in the vertical center of the simulation domain. Within this layer and adjacent to it, the resolution in vertical direction is chosen to $\Delta z = 1$ cm.

The representative fracture-layer permeability $K_{\mathrm{frac}} = 1.645 \times 10^{-12}\mathrm{m}^2$ was estimated using the cubic law and comparing single-phase-flow simulation results for the large scenario to the data from the field-site pumping tests conducted by Schlumberger Carbon Services prior to the field application. The fracture aperture used was $a = 100$ μm, as estimated by Schlumberger Carbon Services resulting in a permeability according to the cubic law of $K_{\mathrm{cubic}} = \frac{a^2}{12} = 8.3 \times 10^{-10}$ m^2 (Hommel et al, 2018). Aperture-weighted averaging of K_{cubic} and the formation permeability of $K = 1.0856 \times 10^{-14}$ m^2 over a total chosen fracture-layer thickness of 5 cm results in an apparent fracture-layer permeability of $K_{\mathrm{frac,app}} = 1.667 \times 10^{-12}\mathrm{m}^2$, which was then reduced to $K_{\mathrm{frac}} = 1.645 \times 10^{-12}$ m^2 to match the pre-application, post-fracturing pumping test data on the large simulation domain.

The fracture-layer porosity is assumed to be identical to the formation porosity of 12%, as the fracture-aperture estimates by Schlumberger Carbon Services were much smaller ($a = 100$ μm) than the vertical resolution used for the fracture layer (1 cm). The critical porosity, at which $K = 0$, in the porosity-permeability relation is estimated to be $\phi_{\mathrm{crit}} = 0.1$, based on the ϕ_{crit} previously fitted for sandstone cores of similar sandstones with comparable initial permeability (Hommel et al, 2013). The computational grid is refined towards the well and around the fracture, see Figure 5. The initial conditions are chosen as hydrostatic pressure distribution with a pressure of 1.79×10^6 Pa for the simulations done prior to the field demonstration (2014) and 3.34×10^6 Pa for the recent (2018) simulations of the field application at the vertical center of the domain. The latter value is higher because it accounts for the filling of the well with water up to the surface.

The initial concentrations (in mole fractions) of the various chemical species are zero except for inorganic carbon $x_{\mathrm{C_{io}}} = 1.79 \times 10^{-7}$ as well as Na^+ and Cl^-, which are both set to $x_{\mathrm{Na}} = x_{\mathrm{Cl}} = 0.007$ to match the formation salinity of 24 g/l reported in Cunningham et al (2014). All other components are assumed not to be present initially. The boundary conditions are set to no-flow boundaries, except for the injection into the fracture layer at the inner radius and a Dirichlet boundary condition for the entire outer radius, which is set to the initial values, except for the pressure in the 2018 simulations. For the 2018 simulations of the actual field application, a simple flow simulation, without component transport and reactions, in a large, 10 km radius domain is used to determine the time-dependent pressure for the Dirichlet boundary condition at the outer radius of the smaller simulation domain for the MICP simulations. Additionally, the simulation domain for MICP was increased to a 50 m radius, keeping the height at 8 m, to capture a more significant portion of the region with high pressure gradients. This is necessary as the pressure signal will obviously propagate much further than the outer radius of the grids used for the simulations in 2014. However, much larger grids than those used are not practical for the MICP simu-

Table 1 Parameters used in the 2014 pre-application simulations which differ from the final calibration values published by Hommel et al (2015).

Parameter	$c_{a,1}$	$c_{a,2}$	ρ_{bio}	k_{ub}
Units	[1/s]	[1/s]	[kg/m^3]	[kg_{urease}/kg_{bio}]
Brief description	Unspecific biomass attachment coefficient	Biomass attachment coefficient to existing biofilm	Biofilm dry density	Urease content of biomass
2014 pre-application	1.5×10^{-5}	5×10^{-6}	10	1×10^{-2}
Hommel et al (2015)	8.3753×10^{-8}	8.5114×10^{-7}	6.9	3.81×10^{-4}

lations due to the complexity and associated computational time of the model, which would, on larger grids, result in impractically long simulation times.

Model Predictions First, the modeled injection strategies and the times of the simulations relative to the field experiment are discussed. We distinguish between the pre-experiment simulations, done in 2014, and the post-experiment simulations, done in 2014 immediately after the field experiment and in 2018. The pre-experiment simulations examined the influence of the injection strategies, “simple” and “ideal”, the size of the domain, “small” and “large”, and radial extent of the fracture, on the simulation results. The post-experiment simulations focused on reproducing the field experiment using the exact (“real”) injection strategy and, additionally for the 2018 simulation, investigating the effect of the model recalibration by Hommel et al (2015) and the outer radius Dirichlet boundary condition on the results.

Two injection strategies were considered during the planning of the 2014 field experiment, one with a low number of injections of long duration each, referred to in the following as the “simple” injection strategy, and one with a high number of short injections, referred to in the following as the “ideal” injection strategy. The latter injection strategy consisted of 7 cell-inoculation and 34 calcium-rich injections, alternating with no-flow periods after the injections allowing for bacterial growth and attachment or reaction. Inoculations were done in the beginning and then prior to overnight no-flow periods and after five of the ten daily calcium-rich injections. Calcium- and cell-free media were injected for a short period before reinoculating to prevent clogging of the immediate vicinity of the well. This injection strategy was chosen to be applied in the field, see the description in Section 4.1, as the model predictions suggested sufficient permeability reduction, see Figure 6, and because the more frequent and faster injections would reduce the risk of unwanted precipitation within the wellbore. A slightly changed strategy was actually applied in the field. This will be referred to as the “real” injection strategy. It was modeled immediately after the field experiment in 2014 and, again, after analyzing the field measurements in 2018. It is similar to the “ideal” strategy but includes sampling and technical problems encountered during the field demonstration as well as decreasing injection rates towards the end of the test. The results for permeability predictions of the model for the three injection strategies simulated in 2014 and the “real” injection strategy simulated in 2018 are shown in Figure 6. The “simple” injection strategy results in almost complete plugging of the high permeability region. For the “ideal” and “real” injection strategies, permeability is reduced mostly in the first 0.5 m to 1 m of the domain, independent of the size of the domain used, when using the 2014 parameter set, see Table 1. Using the best-fit values published by Hommel et al (2015) (Table 1) leads to much less permeability reduction, as much less precipitates are predicted to form, see Figure 7.

The experimental data that can be compared to model results are limited to the recorded injection pressure and a few side-wall cores due to the depth of 340.8 m bgs. Thus, it is difficult to conclude which domain size, boundary conditions, and parameter sets are most accurate. The sensitivity of the model to the estimated formation porosity and permeability, to the assumed fracture-layer porosity and permeability, and to the assumed critical porosity has not been investigated.

A comparison of the “small” and the “large” scenario simulated in 2014 indicates that large simulation domains might only be necessary to investigate the uncertainty in the initial geometry, e.g. extent of the high-permeability layer. Large domains might not be necessary to model MICP for a fixed geometry as the results of both scenarios are quite similar as long as the radius

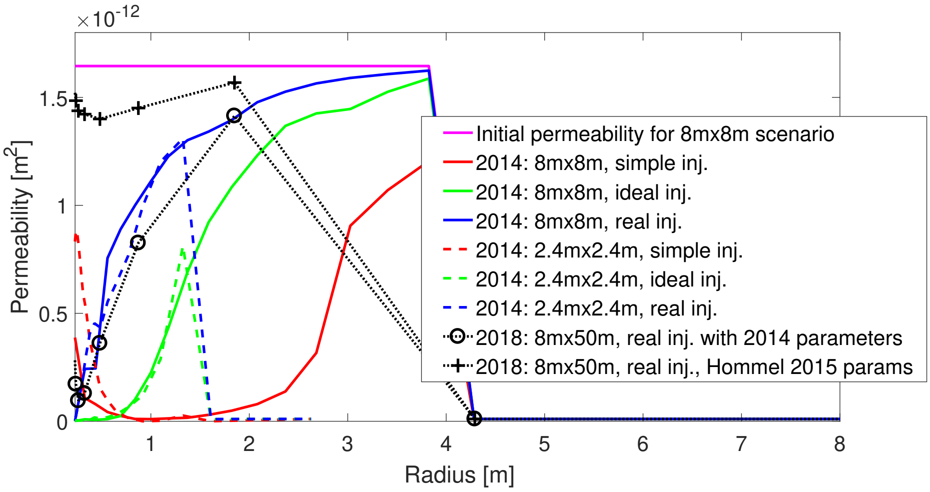

Fig. 6 Permeability along the radius through the high-permeable layer as predicted by simulations for various grids, domain sizes, and injection strategies. Note that the initial permeability on the left is only shown for the "large" 8 m×8 m scenario and that for the "small" 2.4 m×2.4 m scenario, the initial high permeability only extends to a radius of 1.6 m.

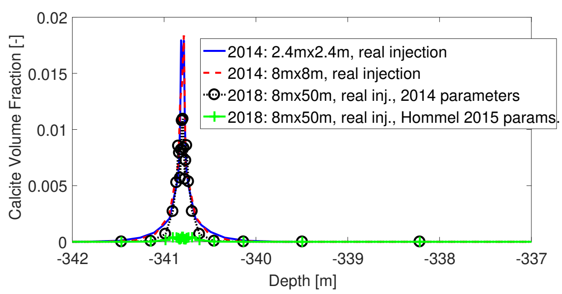

Fig. 7 Calcite volume fractions at the inner boundary over depth predicted by simulations on various simulation domain sizes. The high-permeable layer into which is injected is situated at 340.8 m below surface.

is smaller than the extent of the "small" scenario's high-permeability layer, see Figure 6, when using identical parameter sets. Equally, even when using the further increased domain (8 m×50 m) and a dynamic pressure boundary condition in the 2018 simulations, the results for the biomass (not shown) and calcite distribution do not change significantly compared to the simulations of 2014 with a fixed equilibrium hydrostatic pressure boundary condition, when using identical parameters, see Figure 7. This is a result of the source and sink terms in the model for MICP being almost independent of the absolute value of the pressure. It influences the reaction terms only indirectly by the minor pressure-dependency of the apparent dissociation constants, see Hommel et al (2015). Only the pressure gradient has a significant influence on the detachment rate of biomass, but as the injection is treated as a Neumann boundary, the near-well-bore pressure gradients are independent of the absolute pressure values set at the Dirichlet boundary condition. The simulation results using the planned ("ideal") injection strategy match the field-application results very well, as they predict plugging after 25 Ca^{2+} -rich and 6 biomass injections and also the "real" injection strategy results in a significant permeability reduction, see Figure 6. Although both biofilm and calcite are assumed to be impermeable, most of the permeability reduction is due to calcite, which, for the "real" injection strategy reaches higher volume fractions ($\phi_{\mathrm{c,max}} \approx 0.02$) compared to the small volume fraction of biofilm ($\phi_{\mathrm{b,max}} \approx 0.0006$). However, we have to note that using the updated parameter values from (Hommel et al, 2015) that were the best to model the calibration column experiments did not improve the agreement between the model results and the field-scale experiment. On the contrary, biofilm and calcite volume fractions are reduced and no significant plugging is predicted by the model using this parameter set, see Figure 6 and 7.

It is currently not possible to explicitly verify the simulation results for permeability shown in Figure 6 due to the lack of data. However, side-wall cores, discussed in Section 4.1, collected a year after the field application at 1.8 m above the injection show biomineralized calcite. This compares quite well with the model results of $CaCO_3$ reaching roughly 1 m above and below the fracture layer, see Figure 7. Especially, when considering that the scenarios investigated assume, except for the high-permeable fracture layer, homogeneous initial porosity and permeability without any vertical preferential flow paths. Similarly to calcite, most biomass (not shown here) is concentrated in the high-permeable layer, as in the medium-scale sandstone core in Figure 4.

Another parameter that can be compared between the field application and simulation results is the injection pressure, which is the downhole pressure at the elevation of the entrance to the fracture. In the simulation, the injection pressure is strongly influenced by the Dirichlet pressure boundary condition set at the outer radius. Figure 8 shows the pressure increase due to the total of 30 individual pulses of inoculum or mineralization medium injection and the pressure decrease after each injection. Also, due to the permeability decrease after 40 h, the injection pressure does not relax as fast as during the previous injections, leading to the increase in injection pressure, which was also observed in the field (Phillips et al, 2016). The simulation results, even the recent 2018, with dynamic pressure boundary conditions, are still significantly lower than the maximum pressures measured in the field which were measured to be between $\approx 7 \times 10^6$ and $\approx 8 \times 10^6$ Pa (not shown in Figure 8). Unfortunately, the pressure measurements in the field focused mainly on the maximum pressure peaks during each of the individual injections to avoid potential for damaging the equipment used or refracturing the formation. No continuous pressure measurements were recorded which would be comparable with the simulation data. The general trend in the pressures is matched qualitatively with the gradual increase in pressures as the application proceeded and a pronounced pressure peak at the end of the third day. The difference between the 2014 and 2018 simulations highlights the difficulty of choosing realistic pressure boundary conditions for such field application simulations. However, the pressure has no significant influence on the calculated volume fractions of biofilm (not shown here) or calcite and, therefore, on porosity and permeability, see Figure 6 and 7, as the (bio-)geochemical source and sink terms are not pressure-dependent except for the apparent dissociation constants, see Hommel et al (2015). Thus, the effect of pressure on the simulation results is almost completely limited to the hydraulic part of the model. And, not the absolute value of the pressure is relevant, but rather the injection-dependent pressure gradient.

While the data do not allow an accurate quantitative comparison with the simulation results, there is still encouraging qualitative agreement between simulation results and corresponding field-scale observation of three key system responses. First, we determined that the model prediction of 25 calcium-rich pulses necessary to achieve fracture plugging compared very well with the field observation of 24 calcium-rich pulses. Also, side wall coring revealed that calcite deposits extended roughly one meter above and below the fracture layer, which compares favorably with model results. In addition, the profile of simulated downhole injection pressure compared favorably during periods where actual downhole pressure was measured, especially during the third day when clogging began to occur in the field (Section 4.1).

5 Conclusions

5.1 The State of the MICP Model so far

The long-term goal of this research is to develop biomineralization-based technologies for sealing preferential flow pathways near well-bores and other applications of permeability modification in the subsurface. The history of development of our MICP model clearly demonstrates that a close synergy between laboratory experimentation at different scales and corresponding simulation model development is highly desirable to realize a successful application at the field scale. Joint experimental investigation and model development as discussed in Ebigbo et al (2012) and Hommel et al (2015) has now taken an enormous step towards real field applications. This brings along new challenges. One issue is that the best-fit parameters from Hommel et al (2015) result in only minor precipitation for the field-test setup, while the estimated parameter values used in the 2014 simulations, see Table 1, predict significant clogging. However, both the porous medium as well as the flow field is completely different between the field-test and the calibration setup of Hommel et al (2015). It is difficult to determine exactly why the change in conditions results in another set of parameters seemingly better adapted than the laboratory best-fit parameters. However, it has to be noted that the values of the fitting parameters of the model are strongly correlated (Hommel et al, 2015), which would require a whole set of well-controlled experiments in the relevant porous media and at various scales with more measurements of different kind, all tailored to fulfill the demands of the model to identify a unique set of best-fit parameters. This is clearly our vision for future studies.

Inconsistencies between laboratory and field scale could also possibly arise from local, sub-REV-scale heterogeneities in the field which could result in apparently different kinetics at the modeled resolution as discussed in Burr et al (1994); or such discrepancies might be caused by processes, which have behavior at the laboratory scale that is different than at the field scale, or different behavior in different porous media. The effects from different porous media, e.g. from different pore-size distributions, different pore morphologies or chemical compositions etc., might be addressed by rigorous upscaling of MICP from the pore scale to larger scales. This could possibly lead to upscaled porous medium-dependent parameterizations of the processes for MICP

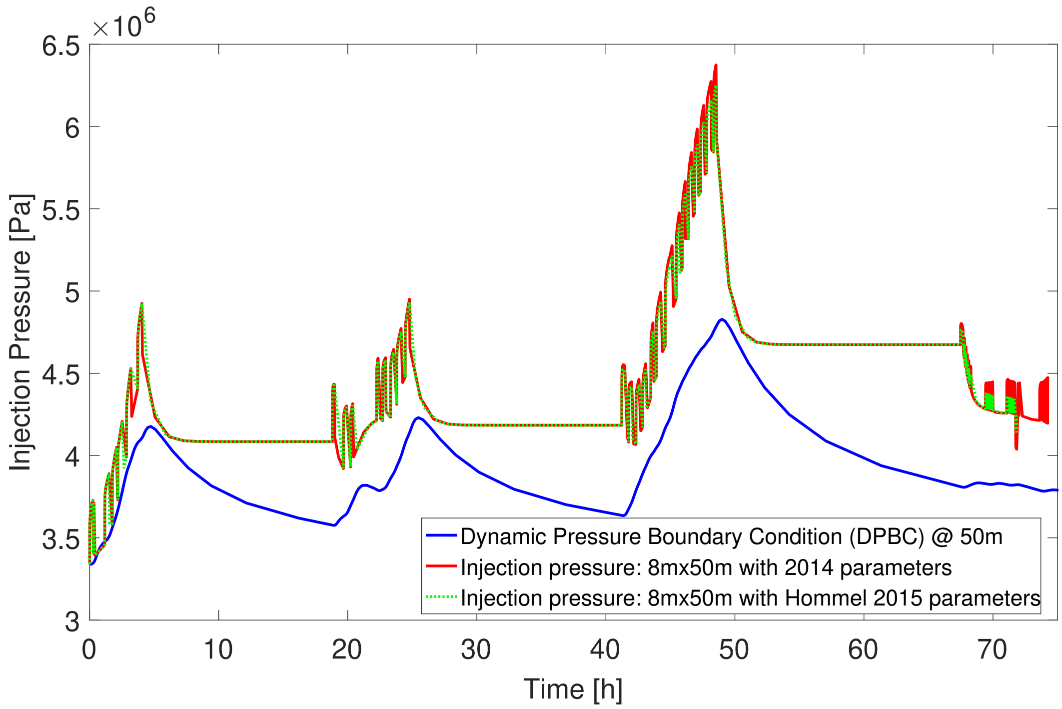

Fig. 8 Injection pressures as predicted by the model for the "real" injection strategy compared to each other and the dynamic pressure boundary condition pressures set for the 2018 simulations. The dynamic pressure set as Dirichlet boundary condition was determined from simple injection simulations on the same geometry, but a radial extent of 10 km.

similar to the studies of e.g. Bringedal et al (2016); Peszyńska et al (2016); Kumar et al (2011); van Noorden et al (2010); Bottero et al (2013, 2010); Heße et al (2009). Nonetheless, at the field scale, there will always be an insufficient amount of information for upscaling. Hence, some degree of parameter fitting is always to be expected. Rigorous upscaling is important to obtain the appropriate functional form of constitutive relationships.

What we consider important for investigating the upscaling of MICP processes between the laboratory and the field scale, is a close cooperation between experimentalists and modelers, as demonstrated in this study and others, e.g. by Nassar et al (2018), and, very importantly, more well-controlled larger-scale experiments such as those conducted by van Paassen et al (2010). A second, equally important, issue is that information on the setup is drastically reduced compared to well-controlled laboratory work, thus complicating determination of correct initial and boundary conditions or other properties of the simulation setup such as the initial distribution of porosity and permeability. Due to this uncertainty in the parameters, it is important to reduce the computational effort of the model for future applications to enable statistical assessment of the effects of the unknown porosity and permeability and, probably to some degree, their heterogeneous distribution. There are various means to achieve this, e.g. local grid refinement, improving the time stepping (e.g. Carrayrou et al, 2010), reducing the coupling between the mass balance equations of different components by improving or changing the numerical scheme (e.g. Hoffmann et al, 2012; Kumar et al, 2011; Kräutle and Knabner, 2007, 2005), the use of a multi-scale approach (e.g. Hajibeygi et al, 2008; Jenny et al, 2005).

While the chosen size of the model domain and the corresponding spatial resolution of the computational grid have only minor influence on the calculated volume fractions of biofilm and precipitated calcite, and thus on the change in porosity and permeability, this does not hold for the predicted pressures. This study has shown that the absolute values of pressure due to the injections are strongly influenced by the pressure boundary condition. The mathematical solution for the pressure in systems of low compressibility behaves approximately elliptic, thus pressure signals travel extremely fast and constant values of pressure at Dirichlet boundaries always limit it. Such effects are also discussed e.g. by Schäfer et al (2012); Birkhölzer et al (2009) for CO_2 storage in deep saline aquifers. Accordingly, the spatial scale of the pressure footprint due to injection is typically much larger than the spatial scale of the induced reactive transport during MICP, which is the area of focus during sealing. The computationally expensive

MICP model usually limits the size of problem. However, it could be beneficial to employ a multi-physics approach, e.g. by coupling the near-well region with MICP to an outer far-field region where only the hydraulics are modeled with a flow model. Or one could apply an analytical solution, similar to the multi-physics approach of e.g. Faigle et al (2014, 2015) or the mortar-space upscaling by e.g. Peszyńska et al (2002).

5.2 Future Applications and Plans for Further Model Improvement

Research on MICP and related applications is continuing in our work groups, now focusing primarily on field-scale sealing of near-well-bore delaminations, fractures, voids and other unrestricted flow channels through well-bore cement. These preferential flow paths can result in lost zonal isolation leading to deleterious flow of fluids between zones or to the surface with multiple potential negative impacts including: loss of resource production, reduction of sweep efficiency in EOR operations, and regulatory non-compliance. Our next steps planned are to model well-bore cement sealing related to unconventional oil and gas recovery and CO_2 sequestration for projects which are currently underway.

For those applications, several further improvements of the model are crucial. First, the computational efficiency of the model should be increased whenever possible to enable the use of larger simulation domains or more refined grids. Also a larger number of simulation runs, in the context of analyses of scenarios, parameter sensitivities, and uncertainties, is important on the field scale to address the inherent uncertainty related to the lack of information and data at the field scale. Second, the model should be thoroughly validated and, if necessary, re-calibrated to well-controlled, large-scale, full 3D, radial flow experiments to investigate the apparent scale dependence of some model parameters. In particular, it should be investigated why the best-fit parameters for the quasi-1D sand column setups seem to underestimate the precipitation of calcite in 3D radial setups in sandstone. Third, the impact of MICP on the two-phase flow properties needs to be included into the model, as the mentioned common feature of the application is the potential presence of two fluid phases, where relative permeabilities and capillary pressures are essential to have for reliable description of flow. Fourth, the model should also be able to predict the increase in mechanical strength due to MICP, which has been shown in experiments, and could be used to increase the stability of cap-rocks.

Appendix

This appendix provides the reactive source and sink terms in the model for MICP used in this study. In the following tables, we refer to the components (water (w), inorganic carbon (ic), sodium (Na), chloride (Cl), calcium (Ca), urea (u), ammonium/ammonia (a), substrate (s), oxygen (O_2), and suspended biomass(sb)) and solid phase (biofilm (b) and calcite (c)) with the respective super- or subscripts.

Sodium and chloride do not take part in any of the reactions directly, which is why $q^{\mathrm{Na}} = q^{\mathrm{Cl}} = 0$. However, they represent the effect of the presence of ions in the aqueous phase on the fluid properties density and viscosity according to the salinity dependent relations given in Batzle and Wang (1992) and on the activity coefficients of the reacting components calculated using Pitzer equations according to Millero et al (1984); Wolf et al (1989); Clegg and Whitfield (1995), as discussed in detail in Ebigbo et al (2012). Also calcium is considered to contribute to salinity and ionic strength. All ions are considered in the charge balance used to determine the pH and the dissociation of total inorganic carbon and ammonia/ammonium.

Table 2 gives all reactive source and sink terms composed of the rates kinetics of the biogeochemical reactions considered in the model. The parameters used to calculated the source and sink terms and rate kinetics are (see also Table 3 for their values): M^{κ} is the molar mass of κ, Y the growth yield coefficient, F the ratio of oxygen to substrate used for growth, k_{urease} the maximum activity of urease, k_{ub} the mass ratio of urease to biofilm, ρ_{b} the density of biofilm, m^{κ} the molality of κ calculated from the mole fraction x_{w}^{κ} and the water-phase properties, K_{u} the half-saturation coefficients for ureolysis, k_{prec} and n_{prec} are empirical precipitation parameters, $k_{\mathrm{diss},1}$, $k_{\mathrm{diss},2}$, and n_{diss} are dissolution parameters, $A_{\mathrm{sw},0}$ is the initial interfacial area of solid and water phase, a_{c} the specific surface area of calcite, K_{sp} the calcite solubility product and γ_{κ} the activity coefficients of κ calculated using Pitzer equations (Millero et al, 1984; Wolf et al, 1989; Clegg and Whitfield, 1995) k_{μ} the maximum specific growth rate, $C_{\mathrm{w}}^{\mathrm{s}}$ and $C_{\mathrm{w}}^{\mathrm{O_2}}$ are the mass concentrations of substrate and oxygen, calculated from the mole fraction x_{w}^{κ} and the water-phase properties, K_{s} and $K_{\mathrm{O_2}}$ the half-saturation coefficients for substrate and oxygen, respectively, b_0 is the endogenous decay rate, K_{pH} an empirical constant accounting for increased bacterial inactivation at non-optimal pH $c_{\mathrm{a},1}$ a general first order attachment coefficient, $c_{\mathrm{a},2}$ a attachment coefficient for preferential attachment to existing biofilm, c_{d} the first order coefficient for detachment due to shear stress and $|\nabla p_\mathrm{w} - \rho_\mathrm{w}\mathbf{g}|$ the absolute value of the potential gradient.

Code availability The numerical simulator DuMu$^\mathrm{X}$ used in this study can be obtained at `http://www.dumux.org/download.php`. The specific code used is available at `https://git.iws.uni-stuttgart.de/dumux-pub/hommel2018a` for the 2018 simulations and `https://git.iws.uni-stuttgart.de/dumux-pub/Shigorina2014a` for the 2014 simulations.

Acknowledgements The International Research Training Group NUPUS, funded by the German Research Foundation (DFG) is acknowledged for enabling the model development through funding between the years 2007 and 2016. Further, we acknowledge the DFG for funding ongoing research related to this study in the grants HO6055/1-1 and within the Collaborative Research Center 1313. Funding for the laboratory and field MICP experimental work was provided by two US Department of Energy grants: DE-FE0004478, "Advanced CO2 Leakage Mitigation using Engineered Biomineralization Sealing Technologies" and DE-FE000959, "Field Test and Evaluation of Engineered Biomineralization Technology for Sealing Existing Wells" with matching support from Southern Company Generation and Shell International Exploration and Production B.V. Additional financial support was also provided by DOE DE-FG02-13ER86571 and NSF Award No. DMS0934696. Any opinions, findings, conclusions, or recommendations expressed herein are those of the authors and do not necessarily reflect the views of the Department of Energy (DOE).

References

Bachmeier KL, Williams AE, Warmington JR, Bang SS (2002) Urease activity in microbiologically-induced calcite precipitation. Journal of Biotechnology 93(2):171–81

Barkouki TH, Martinez BC, Mortensen BM, Weathers TS, De Jong JD, Ginn TR, Spycher NF, Smith RW, Fujita Y (2011) Forward and inverse biogeochemical modeling of microbially induced calcite precipitation in half-meter column experiments. Transport in Porous Media 90(1):23–39, DOI 10.1007/s11242-011-9804-z

Bastian P, Blatt M, Dedner a, Engwer C, Klöfkorn R, Kornhuber R, Ohlberger M, Sander O (2008a) A generic grid interface for parallel and adaptive scientific computing. Part II: Implementation and tests in DUNE. Computing (Vienna/New York) 82(2-3):121–138, DOI 10.1007/s00607-008-0004-9

Bastian P, Blatt M, Dedner a, Engwer C, Klöfkorn R, Ohlberger M, Sander O (2008b) A generic grid interface for parallel and adaptive scientific computing. Part I: Abstract framework. Computing (Vienna/New York) 82(2-3):103–119, DOI 10.1007/s00607-008-0003-x

Batzle M, Wang Z (1992) Seismic Properties of Pore Fluids. Geophysics 57(11):1396–1408, DOI 10.1190/1.1443207

Birkhölzer JT, Zhou Q, Tsang CF (2009) Large-scale impact of CO_2 storage in deep saline aquifers: A sensitivity study on pressure response in stratified systems. International Journal of Greenhouse Gas Control 3(2):181–194

Bottero S, Picioreanu C, Enzien MV, Van Loosdrecht M, Bruining J, Heimovaara T (2010) Formation Damage and Impact on Gas Flow Caused by Biofilms Growing Within Proppant Packing Used in Hydraulic Fracturing. Society of Petroleum Engineers DOI 10.2118/128066-MS

Bottero S, Storck T, Heimovaara TJ, van Loosdrecht MC, Enzien MV, Picioreanu C (2013) Biofilm development and the dynamics of preferential flow paths in porous media. Biofouling 29(9):1069–1086, DOI 10.1080/08927014.2013.828284

Bringedal C, Berre I, Pop IS, Radu FA (2016) Upscaling of Non-isothermal Reactive Porous Media Flow with Changing Porosity. Transport in Porous Media 114(2):371–393, DOI 10.1007/s11242-015-0530-9

Burbank MB, Weaver TJ, Green TL, Williams BC, Crawford RL (2011) Precipitation of Calcite by Indigenous Microorganisms to Strengthen Liquefiable Soils. Geomicrobiology Journal 28(4):301–312, DOI 10.1080/01490451.2010.499929

Burr DT, Sudicky EA, Naff RL (1994) Nonreactive and reactive solute transport in three-dimensional heterogeneous porous media: Mean displacement, plume spreading, and uncertainty. Water Resources Research 30(3):791–815, DOI 10.1029/93WR02946

Carrayrou J, Hoffmann J, Knabner P, Kräutle S, de Dieuleveult C, Erhel J, Van der Lee J, Lagneau V, Mayer KU, MacQuarrie KTB (2010) Comparison of numerical methods for simulating strongly nonlinear and heterogeneous reactive transport problems?the MoMaS benchmark case. Computational Geosciences 14(3):483–502, DOI 10.1007/s10596-010-9178-2

Chou L, Garrels RM, Wollast R (1989) Comparative study of the kinetics and mechanisms of dissolution of carbonate minerals. Chemical Geology 78:269–282

Clegg SL, Whitfield M (1995) A chemical model of seawater including dissolved ammonia and the stoichiometric dissociation constant of ammonia in estuarine water and seawater from -2 to 40°C. Geochimica et Cosmochimica Acta 59(12):2403–2421

Connolly JM, Kaufman M, Rothman A, Gupta R, Redden G, Schuster M, Colwell F, Gerlach R (2013) Construction of two ureolytic model organisms for the study of microbially induced calcium carbonate precipitation. Journal of Microbiological Methods

Table 2 Component-specific reactive source and sink terms of the model used in this study. For details, see Hommel et al (2015) and Ebigbo et al (2012). The parameters values are given in Table 3

Component	Source term		Rates
Water	q^{w}	$=$	0
Inorganic carbon	q^{ic}	$=$	$r_{\mathrm{diss}} - r_{\mathrm{prec}} + r_{\mathrm{urea}}$
Sodium	q^{Na}	$=$	0
Chloride	q^{Cl}	$=$	0
Calcium	q^{Ca}	$=$	$r_{\mathrm{diss}} - r_{\mathrm{prec}}$
Urea	q^{u}	$=$	$-r_{\mathrm{urea}}$
Ammonia/ammonium	q^{a}	$=$	$2r_{\mathrm{urea}}$
Substrate	q^{s}	$=$	$-\frac{r_{\mathrm{g}}^{\mathrm{sb}}+r_{\mathrm{g}}^{\mathrm{b}}}{M^{\mathrm{s}}Y}$
Oxygen	$q^{\mathrm{O_2}}$	$=$	$-F\frac{r_{\mathrm{g}}^{\mathrm{sb}}+r_{\mathrm{g}}^{\mathrm{b}}}{M^{\mathrm{O_2}}Y}$
Suspended biomass	q^{sb}	$=$	$\frac{r_{\mathrm{g}}^{\mathrm{sb}}-r_{\mathrm{b}}^{\mathrm{sb}}-r_{\mathrm{a}}+r_{\mathrm{d}}}{M^{\mathrm{sb}}}$
Biofilm	q^{b}	$=$	$\frac{r_{\mathrm{g}}^{\mathrm{b}}-r_{\mathrm{b}}^{\mathrm{b}}+r_{\mathrm{a}}-r_{\mathrm{d}}}{M^{\mathrm{b}}}$
Calcite	q^{c}	$=$	$r_{\mathrm{prec}} - r_{\mathrm{diss}}$
Ureolysis rate	r_{urea}	$=$	$k_{\mathrm{urease}}k_{\mathrm{ub}}\rho_{\mathrm{b}}\phi_{\mathrm{b}}\frac{m^{\mathrm{u}}}{K_{\mathrm{u}}+m^{\mathrm{u}}}$
Precipitation rate of calcite	r_{prec}	$=$	$k_{\mathrm{prec}}A_{\mathrm{sw}}\left(\Omega-1\right)^{n_{\mathrm{prec}}};\ \Omega \geq 1$
Dissolution rate of calcite	r_{diss}	$=$	$\left(k_{\mathrm{diss},1}m_{\mathrm{H^+}} + k_{\mathrm{diss},2}\right)A_{\mathrm{cw}}\left(\Omega-1\right)^{n_{\mathrm{diss}}};\ \Omega < 1$
Interfacial area solid and water	A_{sw}	$=$	$A_{\mathrm{sw},0}\left(1-\frac{\phi_{\mathrm{c}}}{\phi_0}\right)^{\frac{2}{3}}$
Interfacial area calcite and water	A_{cw}	$=$	$\min\left(A_{\mathrm{sw}}, a_{\mathrm{c}}\phi_{\mathrm{c}}\right)$
Saturation state of calcite	Ω	$=$	$\frac{m^{\mathrm{Ca^{2+}}}\gamma_{\mathrm{Ca^{2+}}}m^{\mathrm{CO_3^{2-}}}\gamma_{\mathrm{CO_3^{2-}}}}{K_{\mathrm{sp}}}$
Growth rate of biofilm	$r_{\mathrm{g}}^{\mathrm{b}}$	$=$	$\mu_{\mathrm{g}}\phi_{\mathrm{b}}\rho_{\mathrm{b}}$
Growth rate of suspended biomass	$r_{\mathrm{g}}^{\mathrm{sb}}$	$=$	$\mu_{\mathrm{g}}C_{\mathrm{w}}^{\mathrm{sb}}S_{\mathrm{w}}\phi$
Specific growth rate	μ_{g}	$=$	$k_{\mu}Y\frac{C_{\mathrm{w}}^{\mathrm{s}}}{K_{\mathrm{s}}+C_{\mathrm{w}}^{\mathrm{s}}}\frac{C_{\mathrm{w}}^{\mathrm{O_2}}}{K_{\mathrm{O_2}}+C_{\mathrm{w}}^{\mathrm{O_2}}}$
Decay rate of biofilm	$r_{\mathrm{b}}^{\mathrm{b}}$	$=$	$\left(b_0+\frac{r_{\mathrm{prec}}M^{\mathrm{CaCO_3}}}{\rho_{\mathrm{c}}(\phi+\phi_{\mathrm{b}})}\right)\phi_{\mathrm{b}}\rho_{\mathrm{b}}$
Decay rate of suspended biomass	$r_{\mathrm{b}}^{\mathrm{sb}}$	$=$	$b_0\left(1+\frac{K_{\mathrm{pH}}}{\left(m^{\mathrm{H^+}}\right)^2}\right)C_{\mathrm{w}}^{\mathrm{sb}}S_{\mathrm{w}}\phi$
Attachment rate of biomass	r_{a}	$=$	$\left(c_{\mathrm{a},1}+c_{\mathrm{a},2}\phi_{\mathrm{b}}\right)C_{\mathrm{w}}^{\mathrm{sb}}S_{\mathrm{w}}\phi$
Detachment rate of biomass	r_{d}	$=$	$\left(c_{\mathrm{d}}\left(\phi S_{\mathrm{w}}\left\|\nabla p_{\mathrm{w}}-\rho_{\mathrm{w}}\mathbf{g}\right\|\right)^{0.58}+\frac{\phi_{\mathrm{b}}}{\phi_0-\phi_{\mathrm{c}}}\mu_{\mathrm{g}}\right)\phi_{\mathrm{b}}\rho_{\mathrm{b}}$

94(3):290–299, DOI 10.1016/j.mimet.2013.06.028

Cunningham AB, Phillips AJ, Troyer E, Lauchnor EG, Hiebert R, Gerlach R, Spangler LH (2014) Wellbore leakage mitigation using engineered biomineralization. Energy Procedia 63:4612–4619, DOI 10.1016/j.egypro.2014.11.494

Cuthbert MO, McMillan LA, Handley-Sidhu S, Riley MS, Tobler DJ, Phoenix VR (2013) A field and modeling study of fractured rock permeability reduction using microbially induced calcite precipitation. Environmental Science & Technology 47(23):13637–13643, DOI 10.1021/es402601g

Ebigbo A, Helmig R, Cunningham AB, Class H, Gerlach R (2010) Modelling biofilm growth in the presence of carbon dioxide and water flow in the subsurface. Advances in Water Resources 33(7):762–781, DOI 10.1016/j.advwatres.2010.04.004

Ebigbo A, Phillips AJ, Gerlach R, Helmig R, Cunningham AB, Class H, Spangler LH (2012) Darcy-scale modeling of microbially induced carbonate mineral precipitation in sand columns. Water Resources Research 48(7):W07519, DOI 10.1029/2011WR011714

Faigle B, Helmig R, Aavatsmark I, Flemisch B (2014) Efficient multiphysics modelling with adaptive grid refinement using a MPFA method. Computational Geosciences pp 625–636, DOI 10.1007/s10596-014-9407-1

Faigle B, Elfeel MA, Helmig R, Becker B, Flemisch B, Geiger S (2015) Multi-physics modeling of non-isothermal compositional flow on adaptive grids. Computer Methods in Applied Mechanics and Engineering 292:16–34, DOI 10.1016/j.cma.2014.11.030

Ferris FG, Stehmeier LG, Kantzas A, Mourits FM (1996) Bacteriogenic Mineral Plugging. Journal of Canadian Petroleum Technology 35(8):56–61, DOI

Table 3 Parameter values used for the simulations in 2014 and 2018. In general, for both sets of simulations, the parameter values as published in Hommel et al (2015) were used. However, as the recalibration of the model was not finished during the 2014 simulations, the fitting parameters were different and given in the table in the format parameter 2014 / parameter 2018. These parameters are compared in detail in Table 1.

Param.	Unit	Value	Reference
ρ_c	$\mathrm{kg/m^3}$	2710	Ebigbo et al (2012)
ρ_b	$\mathrm{kg/m^3}$	10 / 6.9	Ebigbo et al (2012) / Hommel et al (2015)
D_w^κ	$\mathrm{m^2/s}$	$\mathbf{1.587 \times 10^{-9}}$	Riquelme et al (2007)
α_l	m	0.025	Frippiat et al (2008)
$A_{\mathrm{sw},0}$	$\mathrm{m^2/m^3}$	5000	Ebigbo et al (2012)
a_c	$\mathrm{m^2/m^3}$	20000	Ebigbo et al (2012)
k_prec	$\mathrm{mol/m^2s}$	1.5×10^{-10}	Zhong and Mucci (1989)
n_prec	-	3.27	Zhong and Mucci (1989)
$k_{\mathrm{diss},1}$	$\mathrm{kg_{H_2O}/m^2s}$	8.9×10^{-1}	Chou et al (1989)
$k_{\mathrm{diss},2}$	$\mathrm{mol/m^2s}$	6.5×10^{-7}	Chou et al (1989)
n_diss	-	1	Flukiger and Bernard (2009)
k_μ	$\mathrm{1/s}$	$\mathbf{4.1667 \times 10^{-5}}$	Connolly et al (2013)
K_s	$\mathrm{kg/m^3}$	7.99×10^{-4}	Taylor and Jaffé (1990)
$K_{\mathrm{O_2}}$	$\mathrm{kg/m^3}$	2×10^{-5}	Hao et al (1983)
Y	-	0.5	Seto and Alexander (1985)
F	-	0.5	Mateles (1971)
b_0	$\mathrm{1/s}$	3.18×10^{-7}	Taylor and Jaffé (1990)
K_pH	$\mathrm{mol^2/kg^2_{H_2O}}$	6.15×10^{-10}	Kim et al (2000)
$c_{\mathrm{a},1}$	$\mathrm{1/s}$	1.5×10^{-5} / 8.3753×10^{-8}	Estimated / Hommel et al (2015)
$c_{\mathrm{a},2}$	$\mathrm{1/s}$	5×10^{-6} / 8.5114×10^{-7}	Estimated / Hommel et al (2015)
c_d	$\mathrm{1/s}$	2.89×10^{-8}	Ebigbo et al (2010)
k_urease	$\mathrm{mol/kgs}$	**706.7**	Lauchnor et al (2015)
K_u	$\mathrm{mol/kg_{H_2O}}$	**0.355**	Lauchnor et al (2015)
k_ub	-	1×10^{-2} / 3.81×10^{-4}	Bachmeier et al (2002) / Hommel et al (2015)

10.2118/96-08-06

Fidaleo M, Lavecchia R (2003) Kinetic study of enzymatic urea hydrolysis in the pH range 4-9. Chemical and Biochemical Engineering Quarterly 17:311–318

Flemisch B, Darcis M, Erbertseder K, Faigle B, Lauser a, Mosthaf K, Müthing S, Nuske P, Tatomir a, Wolff M, Helmig R (2011) DuMu^X: DUNE for multi-{phase,component,scale,physics,...} flow and transport in porous media. Advances in Water Resources 34(9):1102–1112, DOI 10.1016/j.advwatres.2011.03.007

Flukiger F, Bernard D (2009) A new numerical model for pore scale dissolution of calcite due to CO_2 saturated water flow in 3D realistic geometry: Principles and first results. Chemical Geology 265(1-2):171–180, DOI 10.1016/j.chemgeo.2009.05.004

Frippiat CC, Pérez PC, Holeyman AE (2008) Estimation of laboratory-scale dispersivities using an annulus-and-core device. Journal of Hydrology 362(1-2):57–68, DOI 10.1016/j.jhydrol.2008.08.007

Fujita Y, Taylor JL, Gresham TLT, Delwiche ME, Colwell FS, McLing TL, Petzke LM, Smith RW (2008) Stimulation of Microbial Urea Hydrolysis in Groundwater to Enhance Calcite Precipitation. Environ Sci Technol 42(8):3025–3032

Hajibeygi H, Bonfigli G, Hesse MA, Jenny P (2008) Iterative multiscale finite-volume method. Journal of Computational Physics 227(19):8604 – 8621, DOI 10.1016/j.jcp.2008.06.013

Hao OJ, Richard MG, Jenkins D, Blanch HW (1983) The half-saturation coefficient for dissolved oxygen: A dynamic method for its determination and its effect on dual species competition. Biotechnology and Bioengineering 25(2):403–16, DOI 10.1002/bit.260250209

Helmig R (1997) Multiphase Flow and Transport Processes in the Subsurface - A Contribution to the Modeling of Hydrosystems. Springer Verlag

Heße F, Radu F, Thullner M, Attinger S (2009) Upscaling of the advection-diffusion-reaction equation with Monod reaction. Advances in Water Resources 32(8):1336 – 1351, DOI 10.1016/j.advwatres.2009.05.009

Hoffmann J, Kräutle S, Knabner P (2012) A general reduction scheme for reactive transport in porous media. Computational Geosciences 16(4):1081–1099, DOI 10.1007/s10596-012-9304-4

Hommel J, Cunningham AB, Helmig R, Ebigbo A, Class H (2013) Numerical Investigation of Microbially Induced Calcite Precipitation as a Leakage Mitigation Technology. Energy Procedia 40C:392–

397, DOI 10.1016/j.egypro.2013.08.045

Hommel J, Lauchnor EG, Phillips AJ, Gerlach R, Cunningham AB, Helmig R, Ebigbo A, Class H (2015) A revised model for microbially induced calcite precipitation: Improvements and new insights based on recent experiments. Water Resources Research 51(5):3695–3715, DOI 10.1002/2014WR016503

Hommel J, Lauchnor EG, Gerlach R, Cunningham AB, Ebigbo A, Helmig R, Class H (2016) Investigating the Influence of the Initial Biomass Distribution and Injection Strategies on Biofilm-Mediated Calcite Precipitation in Porous Media. Transport in Porous Media 114(2):557–579, DOI 10.1007/s11242-015-0617-3

Hommel J, Coltman E, Class H (2018) Porosity-Permeability Relations for Evolving Pore Space: A Review with a Focus on (Bio-)geochemically Altered Porous Media. Transport in Porous Media, DOI 10.1007/s11242-018-1086-2

Jacques D, Šimůnek J, Mallants D, van Genuchten M (2008) Modelling coupled water flow, solute transport and geochemical reactions affecting heavy metal migration in a podzol soil. Geoderma 145(3):449 – 461, DOI 10.1016/j.geoderma.2008.01.009

Jenny P, Lee S, Tchelepi H (2005) Adaptive Multiscale Finite-Volume Method for Multiphase Flow and Transport in Porous Media. Multiscale Modeling & Simulation 3(1):50–64, DOI 10.1137/030600795

Kim DS, Thomas S, Fogler HS (2000) Effects of pH and trace minerals on long-term starvation of Leuconostoc mesenteroides. Applied and Environmental Microbiology 66(3):976–81

Krajewska B (2017) Urease-aided calcium carbonate mineralization for engineering applications: A review. Journal of Advanced Research DOI 10.1016/j.jare.2017.10.009

Kräutle S, Knabner P (2005) A new numerical reduction scheme for fully coupled multicomponent transport-reaction problems in porous media. Water Resources Research 41(9):W09414, DOI 10.1029/2004WR003624

Kräutle S, Knabner P (2007) A reduction scheme for coupled multicomponent transport-reaction problems in porous media: Generalization to problems with heterogeneous equilibrium reactions. Water Resources Research 43(3):W03429, DOI 10.1029/2005WR004465

Kumar K, van Noorden T, Pop I (2011) Effective Dispersion Equations for Reactive Flows Involving Free Boundaries at the Microscale. Multiscale Modeling & Simulation 9(1):29–58, DOI 10.1137/100804553

Landa-Marbán D, Radu FA, Nordbotten JM (2017) Modeling and simulation of microbial enhanced oil recovery including interfacial area. Transport in Porous Media 120(2):395–413, DOI 10.1007/s11242-017-0929-6

Lauchnor EG, Topp DM, Parker AE, Gerlach R (2015) Whole cell kinetics of ureolysis by Sporosarcina pasteurii. Journal of Applied Microbiology 118(6):1321–1332, DOI 10.1111/jam.12804

Martinez B, De Jong JT, Ginn TR (2014) Biogeochemical reactive transport modeling of microbial induced calcite precipitation to predict the treatment of sand in one-dimensional flow. Computers and Geotechnics 58:1–13, DOI 10.1016/j.compgeo.2014.01.013

Mateles RI (1971) Calculation of the oxygen required for cell production. Biotechnology and Bioengineering 13(4):581–582, DOI 10.1002/bit.260130411

Millero FJ, Milne PJ, Thurmond VL (1984) The solubility of calcite, strontianite and witherite in NaCl solutions at 25°C. Geochimica et Cosmochimica Acta 48:1141–1143, DOI 10.1016/0016-7037(84)90205-9

Minto JM, Tan Q, Lunn RJ, Mountassir GE, Guo H, Cheng X (2018) Microbial mortar-restoration of degraded marble structures with microbially induced carbonate precipitation. Construction and Building Materials 180:44–54, DOI 10.1016/j.conbuildmat.2018.05.200

Mitchell AC, Phillips AJ, Schultz L, Parks S, Spangler LH, Cunningham AB, Gerlach R (2013) Microbial $CaCO_3$ mineral formation and stability in an experimentally simulated high pressure saline aquifer with supercritical CO_2. International Journal of Greenhouse Gas Control 15:86–96, DOI 10.1016/j.ijggc.2013.02.001

Nassar MK, Gurung D, Bastani M, Ginn TR, Shafei B, Gomez MG, Graddy CMR, Nelson DC, DeJong JT (2018) Large-Scale Experiments in Microbially Induced Calcite Precipitation (MICP): Reactive Transport Model Development and Prediction. Water Resources Research 54:480–500, DOI 10.1002/2017WR021488

Nemati M, Voordouw G (2003) Modification of porous media permeability, using calcium carbonate produced enzymatically in situ. Enzyme and Microbial Technology 33(5):635 – 642, DOI 10.1016/S0141-0229(03)00191-1

Nielsen SM, Nesterov I, Shapiro AA (2014) Simulations of microbial-enhanced oil recovery: Adsorption and filtration. Transport in Porous Media 102(2):227–259, DOI 10.1007/s11242-014-0273-z

Nielsen SM, Nesterov I, Shapiro AA (2016) Microbial enhanced oil recovery—a modeling study of the potential of spore-forming bacteria. Computational Geosciences 20(3):567–580, DOI 10.1007/s10596-015-9526-3 van Noorden TL, Pop IS, Ebigbo A, Helmig R (2010) An upscaled model for biofilm growth in a thin strip. Water Resources Research 46(6):W06505, DOI 10.1029/2009WR008217

van Paassen LA, Ghose R, van der Linden TJM, van der Star WRL, van Loosdrecht MCM (2010) Quantifying Biomediated Ground Improvement by Ureolysis: Large-Scale Biogrout Experiment. Journal of Geotechnical and Geoenvironmental Engineering 136(12):1721–1728, DOI {10.1061/(ASCE)GT.1943-5606.0000382}

Peszyńska M, Wheeler MF, Yotov I (2002) Mortar Upscaling for Multiphase Flow in Porous Media. Computational Geosciences 6(1):73–100, DOI 10.1023/A:1016529113809

Peszyńska M, Trykozko A, Iltis G, Schlueter S, Wildenschild D (2016) Biofilm growth in porous media: Experiments, computational modeling at the porescale, and upscaling. Advances in Water Resources 95:288 – 301, DOI 10.1016/j.advwatres.2015.07.008

Phillips AJ, Gerlach R, Lauchnor EG, Mitchell AC, Cunningham AB, Spangler LH (2013a) Engineered applications of ureolytic biomineralization: a review. Biofouling 29(6):715–733, DOI 10.1080/08927014.2013.796550

Phillips AJ, Lauchnor EG, Eldring JJ, Esposito R, Mitchell AC, Gerlach R, Cunningham AB, Spangler LH (2013b) Potential CO_2 leakage reduction through biofilm-induced calcium carbonate precipitation. Environmental Science & Technology 47:142–149, DOI 10.1021/es301294q

Phillips AJ, Eldring J, Hiebert R, Lauchnor EG, Mitchell AC, Cunningham AB, Spangler LH, Gerlach R (2015) Design of a meso-scale high pressure vessel for the laboratory examination of biogeochemical subsurface processes. Journal of Petroleum Science and Engineering 126:55–62, DOI 10.1016/j.petrol.2014.12.008

Phillips AJ, Cunningham AB, Gerlach R, Hiebert R, Hwang C, Lomans BP, Westrich J, Mantilla C, Kirksey J, Esposito R, Spangler LH (2016) Fracture Sealing with Microbially-Induced Calcium Carbonate Precipitation: A Field Study. Environmental Science & Technology 50:4111–4117, DOI 10.1021/acs.est.5b05559

Prommer H, Grassi ME, Davis AC, Patterson BM (2007) Modeling of microbial dynamics and geochemical changes in a metal bioprecipitation experiment. Environmental Science & Technology 41(24):8433–8438, DOI 10.1021/es071123n

Qin C, Hassanizadeh SM, Ebigbo A (2016) Pore-scale network modeling of microbially induced calcium carbonate precipitation: Insight into scale dependence of biogeochemical reaction rates. Water Resources Research 52(11):8794–8810, DOI 10.1002/2016WR019128

Riquelme R, Lira I, Pérez-López C, Rayas JA, Rodríguez-Vera R (2007) Interferometric measurement of a diffusion coefficient: comparison of two methods and uncertainty analysis. Journal of Physics D: Applied Physics 40(9):2769–2776, DOI 10.1088/0022-3727/40/9/015

Schäfer F, Walter L, Class H, Müller C (2012) The regional pressure impact of CO_2 storage: a showcase study from the North German Basin. Environmental Earth Sciences 65(7):2037–2049, DOI 10.1007/s12665-011-1184-8

Seto M, Alexander M (1985) Effect of bacterial density and substrate concentration on yield coefficients. Applied and Environmental Microbiology 50(5):1132–1136

Taylor SW, Jaffé PR (1990) Substrate and biomass transport in a porous-medium. Water Resources Research 26(9):2181–2194, DOI 10.1029/WR026i009p02181

Tebes-Stevens C, Valocchi AJ, VanBriesen JM, Rittmann BE (1998) Multicomponent transport with coupled geochemical and microbiological reactions: model description and example simulations. Journal of Hydrology 209(1):8 – 26, DOI 10.1016/S0022-1694(98)00104-8

Umar M, Kassim KA, Chiet KTP (2016) Biological process of soil improvement in civil engineering: A review. Journal of Rock Mechanics and Geotechnical Engineering 8(5):767 – 774, DOI 10.1016/j.jrmge.2016.02.004

Verma A, Pruess K (1988) Thermohydrological conditions and silica redistribution near high-level nuclear wastes emplaced in saturated geological formations. Journal of Geophysical Research: Solid Earth 93(B2):1159–1173, DOI 10.1029/JB093iB02p01159

Vilcáez J, Li L, Wu D, Hubbard SS (2013) Reactive Transport Modeling of Induced Selective Plugging by Leuconostoc Mesenteroides in Carbonate Formations. Geomicrobiology Journal 30(9):813–828, DOI 10.1080/01490451.2013.774074

van der Vorst HA (1992) BI-CGSTAB: A Fast and Smoothy Converging Variant of BI-CG for the Solution of Nansymmetric Linear Systems. SIAM J Sci Comput 13(2):631–644

Watson Ia, Oswald SE, Mayer KU, Wu Y, Banwart Sa (2003) Modeling kinetic processes controlling hydrogen and acetate concentrations in an aquifer-derived microcosm. Environmental Science and Technology 37(17):3910–3919, DOI 10.1021/es020242u

Whiffin VS, van Paassen La, Harkes MP (2007) Microbial Carbonate Precipitation as a Soil Improvement Technique. Geomicrobiology Journal 24(5):417–423, DOI 10.1080/01490450701436505

van Wijngaarden WK, Vermolen FJ, Meurs GAM, Vuik C (2011) Modelling Biogrout: A new ground improvement method based on microbial-induced carbonate precipitation. Transport in Porous Media 87(2):397–420, DOI 10.1007/s11242-010-9691-8

van Wijngaarden WK, Vermolen FJ, Meurs GAM, Vuik C (2013) A mathematical model for Biogrout. Computational Geosciences 17(3):463–478, DOI 10.1007/s10596-012-9316-0

van Wijngaarden WK, van Paassen LA, Vermolen FJ, van Meurs GAM, Vuik C (2016) A Reactive Transport Model for Biogrout Compared to Experimental Data. Transport in Porous Media 111(3):627–648, DOI 10.1007/s11242-015-0615-5

Wolf M, Breitkopf O, Puk R (1989) Solubility of calcite in different electrolytes at temperatures between 10 and 60°C and at CO_2 partial pressures of about 1 kPa. Geochemical Journal 76:291–301

Zhang T, Klapper I (2010) Mathematical model of biofilm induced calcite precipitation. Water Science and Technology 61(11):2957, DOI 10.2166/wst.2010.064

Zhang T, Klapper I (2011) Mathematical model of the effect of electrodiffusion on biomineralization. International Journal of Non-Linear Mechanics 46(4):657–666, DOI 10.1016/j.ijnonlinmec.2010.12.008

Zhang T, Klapper I (2014) Critical occlusion via biofilm induced calcite precipitation in porous media. New Journal of Physics 16(5):055009, DOI 10.1088/1367-2630/16/5/055009

Zhong S, Mucci A (1989) Calcite and aragonite precipitation from seawater solutions of various salinities: Precipitation rates and overgrowth compositions. Chemical Geology 78:283–299